Analysis Note for: Dynamical Relative Charge Number Fluctuations Across Multiple Regimes of QCD Matter in Au_{like}+Al and Au+Au Collisions From $\sqrt{s_{NN}}$ = 3.0 - 200 GeV

Terence J. Tarnowsky

(Dated: January 27, 2017)

CONTENTS

I. Au_{like} + Al COLLISIONS

There are different ideas about what projectile is hitting the aluminum beam pipe at $\sqrt{s_{NN}} < 4.5$ GeV. The accelerator physicists at RHIC maintain that Au^{79+} beam halo can not be the dominant source for collisions with the beam pipe. If it were exclusively beam halo, one would expect a relatively isotropic distribution of vertices in the transverse (x − y) plane. There is an asymmetry in the location of events in the x − y vertex distribution, shown in Figure 1.

Several studies were carried out by the authors of "Coulomb effect in Au_{like} + Al collisions at $\sqrt{s_{NN}} = 3.0$, 3.5, and 4.5 GeV to constrain the type of projectile hitting the beam pipe STAR FXT Coulomb Effect paper. It was hypothesized that the beam halo could consist of heavy fragments from Au+H interactions in the warm bore between the D0 and DX magnets, or Au^{78+} ions from electron capture from He-atoms in the RHIC cold bore. Both of these

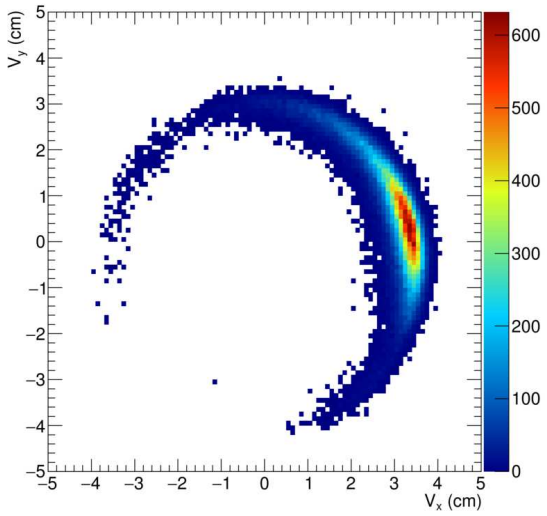

FIG. 1. Distribution of event vertices in the x − y plane for Au_{like}+Al collisions at STAR. The anisotropy in event distribution is visible.

possibilities would be supported by an anisotropic event distribution, due to differential bending in the RHIC magnetic field relative to Au^{79+} ions. Glauber studies and comparisons to produced pion and proton multiplicity distributions concluded that the projectile Z is 80 ± 30, or 80 ± 10, respectively. This is highly consistent with a "Au_{like}" projectile hitting the Al beam pipe.

II. EVENT AND TRACK SELECTION

Because this paper includes data analyzed from collider mode operations, fixed target mode collisions at STAR (FXT), and projectile beam collisions with the aluminum beam pipe, multiple definitions will be discussed depending on which system is being analyzed. When referring to the internal STAR gold foil fixed target it will be denoted as, "FXT".

Throughout this analysis note, minimum-bias data sets were used from RHIC Runs 10, 11, and 14. For collider mode, the centrality of each collision was determined according to the measured charged hadron multiplicity within the pseudorapidity range $|\eta| < 0.5$ (reference multiplicity). In fixed target mode the collision centrality was determined from either produced pions (Au_{like}+Al) or from charged hadron multiplicity (Au+AuFXT and Al+AuFXT). For projectile beams on the FXT the pseudorapidity range used was 0.25 <

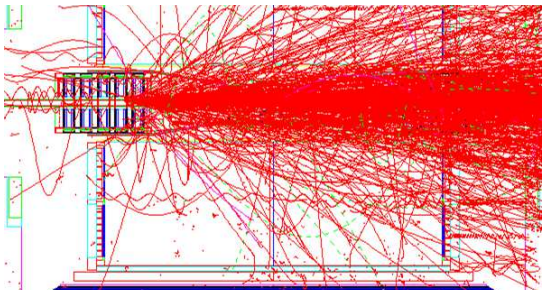

FIG. 2. Schematic of a Au_{like}+Al collision at STAR. Image from: nuclear.ucdavis.edu/ star/protected/FixedTargetPaper/analysisdetails.php

$\eta < 1.75$. For Au_{like}+Al) beam pipe collisions the pseudorapidity range was $0.25 < \eta < 1.75$ for events with negative vertex-z (v_z) position, or $-0.25 > \eta > -1.75$ for events with positive v_z. This corresponded to a region of the STAR acceptance where particle yields were relatively flat across all the fixed target energies. Because the center of mass rapidity (y_{cm}) is so far forward it is not possible to have acceptance cuts that are symmetric about y_{cm}. Studies of asymmetric acceptance cuts about y_{cm} in higher energy Au+Au collisions show there is no change within the TPC acceptance.

The centrality bins were calculated as a fraction of the reference multiplicity distribution starting with the highest multiplicities (most central) to the lowest multiplicities (most peripheral). Nine centrality bins were used: 0-5%, 5-10%,10-20%, 20-30%, 30-40%, 40-50%, 50-60%, 60-70%, and 70-80%.

For collider mode: To ensure nearly uniform detector acceptance and avoid multiplicity biases near the edges of the TPC, cuts were made on the z position of the reconstructed primary vertex. These cuts are listed in Tables I and II for each experimental run. In addition, the radial position of the primary vertex was required to be less than 2 cm. This radial cut is more important in RHIC's low energies runs where the beam spot was relatively large and the beam pipe events were a large source of background. Events must also pass other quality assurance (QA) cuts. Event-wise quantities such as average reference multiplicity, $< \eta >$, $< \phi >$, $< p_T >$, $< \pi >$, $< K >$, etc. are calculated for each run and plotted as a function of run number (time). Events that have quantities that fluctuate beyond two standard deviations from the overall mean value are excluded. Tables I and IIsummarizes the number of events that pass these various QA cuts.

For fixed target mode: To ensure a beam pipe collision in Au_{like}+Al data, a radial cut of

Run	Year	$\sqrt{s_{\rm NN}}$ (GeV)	Species	$\lvert z\rvert$ (cm)	# of Events (millions)
10	2010	7.7	Au+Au	70	3.3
10	2010	11.5	Au+Au	50	6.0
10	2010	39	Au+Au	30	6.3
10	2010	62.4	Au+Au	30	3.7
10	2010	200	Au+Au	30	8.4
11	2011	19.6	Au+Au	30	8.5
11	2011	27	Au+Au	30	20.1
11	2011	200	Au+Au	30	20.0
14	2014	14.5	Au+Au	30	5.1

TABLE I. Summary of collider mode data sets, primary vertex cuts, and the number of good events used in the analysis.

Run	Year	$\sqrt{s_{\rm NN}}$ (GeV)	Species	z (cm)	# of Events (millions)
10	2010	3.0	$\rm Au_{like}$+Al	$80 < \lvert z\rvert < 200$	3.4
10	2010	3.5	$\rm Au_{like}$+Al	$80 < \lvert z\rvert < 200$	2.1
11	2011	3.9	$\rm Au_{like}$+Al	$80 < \lvert z\rvert < 200$	4.1
14	2014	4.5	$\rm Au_{like}$+Al	$80 < \lvert z\rvert < 200$	3.7
15	2015	4.5	Au+Au	$210 < z < 212$	1.2
15	2015	4.9	Al+Au	$210 < z < 212$	3.1

TABLE II. Summary of fixed target mode data sets, primary vertex cuts, and the number of good events used in the analysis.

$2.0 < \rm v_r < 5.0$ cm was used. To ensure a beam pipe collision is traversing the TPC in the correct direction, the sum of the longitudinal momentum ($\rm p_z$) in an event was calculated. For events at negative $\rm v_z$ the $\rm p_z$ is required to positive, and vice-versa. Additionally, for all fixed target systems each event was required to have at least one matched track in the TOF to avoid triggering on pile-up or other out of time events. The FXT events were also verified to have the proper vertex index (0).

Collider $\sqrt{s_{\rm NN}}$ (GeV)	Single Beam $E_{\rm kin}$ (GeV)	Fixed Target $\sqrt{s_{\rm NN}}$ (GeV)	$y_{\rm cm}$	$\mu_{\rm B}$ (MeV)
7.7	3.84	3.0	1.16	721
11.5	5.73	3.5	1.33	667
14.5	7.27	3.9	1.43	633
19.6	9.78	4.5	1.57	589
Au-beam, Au-target	9.78	4.5	1.57	589
Aul-beam, Au-target	11.73	4.9	1.65	562

TABLE III. Summary of collider mode beam parameters and the corresponding fixed target kinematic variables.

Standard STAR track quality cuts were used. Only tracks having more than 15 hits out of a maximum of 45 measurable space points along the trajectory were considered as good. The ratio of the numbers of reconstructed space points to possible space points along the track was required to be greater than 0.52 to avoid the effects of track splitting. Tracks in the TPC were characterized by the distance of closest approach (DCA), which is the distance between the projection of the track at its closest point to the measured event vertex. Particles originating from weak decays can have larger DCAs than the direct primary particles. All tracks were required to have a DCA of less than 1.0 cm. Additional requirements include: the number of dE/dx hits to be greater than 0.

III. PARTICLE IDENTIFICATION

Particle identification was accomplished with both STAR's TPC and TOF detectors. A charged particle's trajectory is deflected by the external magnetic field while traveling inside the TPC gas volume so the magnetic rigidity can be used to determine the particle's momentum. Also, the charged particles interact with the gas and lose energy by ionizing electrons of the gas atoms. This specific ionization energy loss, dE/dx, is a function of the particle momentum and species. The TOF measures the particle's flight time precisely, which is combined with the momentum measurement from the TPC to provide particle identification.

Due to the fact that the TOF has excellent particle identification capability but relatively

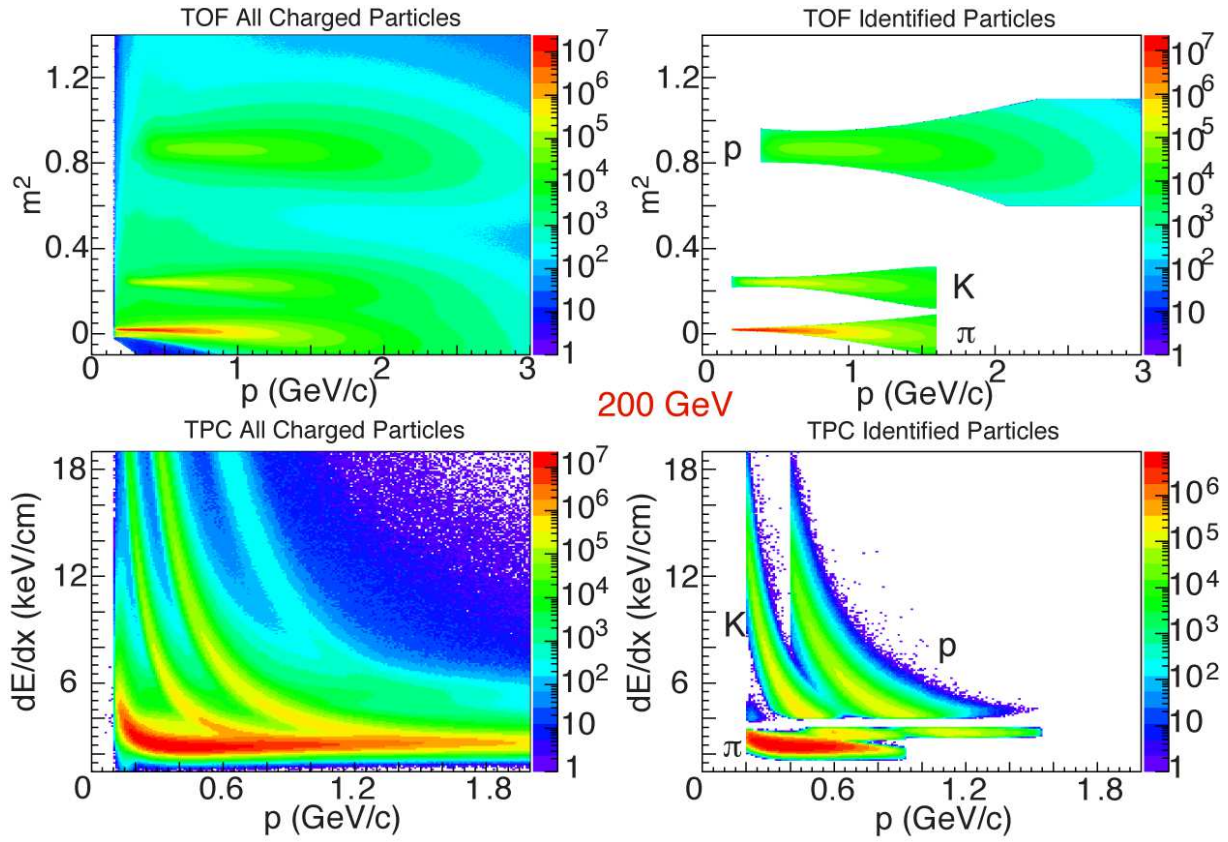

FIG. 3. Upper: m^2 vs. p for all charged particles and identified kaons, pions, and protons using TOF PID. Lower: dE/dx vs. p for all charged particles and identified kaons, pions and protons using TPC PID.

low efficiency, a combined identification method is applied to achieve the maximum efficiency and accuracy. If a particle has a TOF match, we use the particle's velocity β extracted from the time-of-flight, otherwise we switch to the TPC and use its dE/dx to make the identification. Figure 3 shows m^2 vs. p for all charged particles and identified kaons, pions and protons using TOF PID, as well as dE/dx vs. p for all charged particles and identified kaons, pions and protons using TPC PID. For TOF PID, the m^2 method is used, which can be written as

$$m^2 = \frac{p^2}{\gamma^2\beta^2} = (\frac{1}{\beta^2} - 1)p^2 \tag{1}$$

where the β is extracted from the TOF and the momentum information is taken from the TPC. The benefit of this m^2 method is that it does not depend on momentum so

the mean value of each mass distribution should be constant as a function of momentum. The disadvantage is that the method uses the momentum from TPC so the identification uncertainty depends on momentum. In this analysis, we used Gaussian fits to all three mass peaks at each momentum bin, extracted the width from the fits, and only kept tracks that are less than two standard deviations away from the expected m^2 value. A hard cut of $0.6 < m^2 < 1.1$ is also applied to the proton mass peak due to its relatively wide distribution. For identified pions and kaons, we use a momentum cut of $\mathrm{p_T} > 0.2$ GeV/c and $p < 1.8$ GeV/c, while for protons, we increase the lower cut to $\mathrm{p_T} < 0.4$ GeV/c to reduce the number of background protons knocked out from the beam pipe and the detector materials. A $p < 3$ GeV/c upper cut is also used to improve the separation of kaons and protons (compared to pions and kaons) in the high momentum region.

Similarly, for TPC PID, we required that the specific energy loss be less than two standard deviations away from the energy loss predicted for the desired particle species, and would also be more than two standard deviations away from the energy loss predicted for the other particles. The lower $\mathrm{p_T}$ cut for TPC PID is $0.2 < \mathrm{p_T} < 0.6$ GeV/c for pions and kaons, while for protons it is $0.4 < \mathrm{p_T} < 1.0$ GeV/c.

In fixed-target configuration the identified particle cuts have to be changed due to the longitudinal boost of the produced particles. For pions and kaons the minimum $\mathrm{p_T}$ is reduced to 0.15 GeV/c and for protons is reduced to 0.25 GeV/c. The minimum $\mathrm{p_T}$ cuts used in collider mode results in low momentum particles not traveling far enough in pseudorapidity before they curve out of the acceptance.

IV. EXPERIMENTALLY PARAMETRIZED MULTIPLICITIES

The scaling variable used in this paper involves experimentally parameterized multiplicity formulas. These formulas were derived from the energy dependence of the multiplicity across a wide range of energies. The two that apply in the energy range studied here are published by either the PHOBOS or ALICE experiments [1, 2].

$$\frac{2}{\langle \mathrm{N_{part}} \rangle} \frac{\mathrm{dN_{ch}}}{\mathrm{d}\eta} = 0.78 ln(\sqrt{s}) - 0.4, \tag{2}$$

$\sqrt{s_{\rm NN}}$ (GeV)	Species	$\langle N_{\rm part}\rangle$	Centrality
7.7	Au+Au	332.1	0-5%
11.5	Au+Au	334.7	0-5%
14.5	Au+Au	337.3	0-5%
19.6	Au+Au	338.5	0-5%
27.0	Au+Au	338.9	0-5%
39.0	Au+Au	340.0	0-5%
62.4	Au+Au	342.6	0-5%
200.0	Au+Au	350.9	0-5%
4.5	Au+Au	309.8	0-10%
3.0	Au_{like}+Al	92.1	0-10%
3.5	Au_{like}+Al	92.8	0-10%
3.9	Au_{like}+Al	93.2	0-10%
4.5	Au_{like}+Al	93.9	0-10%
2760.0	Pb+Pb	382.8	0-5%

TABLE IV. $\langle N_{\rm part}\rangle$ used to calculate parameterized multiplicities. Values for Au+Au for $\sqrt{s_{\rm NN}}$ >= 7.7 GeV and Pb+Pb at $\sqrt{s_{\rm NN}}$ = 2760 GeV are from [3, 4]. The remaining values were calculated using PHOBOS TGlauber 2.0 [5]

$$\frac{2}{\langle N_{\rm part}\rangle}\frac{dN_{\rm ch}}{d\eta} = 0.77 s^{0.15}, \tag{3}$$

The main parameters in the above formulas are the collision energy of the system and the $\langle N_{\rm part}\rangle$ at a particular energy and centrality. The values of $\langle N_{\rm part}\rangle$ for Au+Au above $\sqrt{s_{\rm NN}}$ = 7.7 GeV were obtained from [3]. For 0-5% central Pb+Pb collisions at ALICE, $N_{\rm part}$ was obtained from [4]. For Au_{like}+Al and Au/Al+AuFXT, Glauber simulations were carried out using the TGlauber 2.0 framework [5]. Additional nucleus parameters were added to the source code, as needed for any species that was absent.

V. $\nu_{\mathrm{dyn},+-}$

A. Calculating $\nu_{\mathrm{dyn},+-}$ Directly and Bin-by-Bin

ν_{dyn} is defined as,

$$\nu_{\mathrm{dyn,AB}} = \frac{\langle N_{\mathrm{A}}(N_{\mathrm{A}}-1)\rangle}{\langle N_{\mathrm{A}}\rangle^2} + \frac{\langle N_{\mathrm{B}}(N_{\mathrm{B}}-1)\rangle}{\langle N_{\mathrm{B}}\rangle^2} - 2\frac{\langle N_{\mathrm{A}}N_{\mathrm{B}}\rangle}{\langle N_{\mathrm{A}}\rangle\langle N_{\mathrm{B}}\rangle}, \tag{4}$$

The calculation of ν_{dyn} has been done via two different methods to verify the result. "Method 1" is the direct method that calculates (inside a centrality bin) the sums and averages that are inputs to the formula for ν_{dyn} (Equation 4). It is binned in terms of the defined centrality (e.g. 0-5%, 0-10%, 10-20%, etc.) "Method 2" is a bin-by-bin calculation as a function of $\mathrm{N_{ch}}$, which is then summed up across a centrality bin and normalized by the number of events in that bin to create a weighted average. This is the same method used to extract p_T and charge fluctuations, as well as forward-backward (FB) correlations [6]. If ν_{dyn} were sensitive to the width of a centrality bin, these two methods would produce disparate results. It is shown in Table VI A that ν_{dyn} is insensitive to the width of the centrality bin and the two methods produce almost identical results if event statistics are large enough to fully populate all of the unit size $\mathrm{N_{ch}}$ bins. Because Method 2 uses unit size bins, with low event statistics there can be large fluctuations using this method, while Method 1 stabilizes faster due to initial averaging over a finite width centrality bin. This can be seen particularly in the results for $\mathrm{Au_{like}}$+Al. Method 1 provides the results used in the paper.

B. Statistical Error Determination

The statistical error for $\nu_{\mathrm{dyn},+-}$ is calculated using a sub-sample method. There is also an analytical expression for the statistical error on ν_{dyn} [7]. Both methods were previously shown to produce similar error values.

$\sqrt{s_{\rm NN}}$ (GeV)	Species	$\nu_{\rm dyn,+-}$ Method 1	$\nu_{\rm dyn,+-}$ Method 2	Centrality
7.7	Au+Au	-5.40e-03 ± 5.50e-05	-5.45e-03 ± 6.40e-05	0-5%
11.5	Au+Au	-4.23e-03 ± 5.42e-05	-4.29e-03 ± 3.67e-05	0-5%
14.5	Au+Au	-3.76e-03 ± 2.26e-05	-3.80e-03 ± 3.54e-05	0-5%
19.6	Au+Au	-3.39e-03 ± 1.57e-05	-3.47e-03 ± 2.22e-05	0-5%
27.0	Au+Au	-3.03e-03 ± 1.51e-05	-3.05e-03 ± 1.34e-05	0-5%
39.0	Au+Au	-2.66e-03 ± 2.66e-05	-2.68e-03 ± 1.93e-05	0-5%
62.4	Au+Au	-2.38e-03 ± 4.31e-05	-2.41e-03 ± 2.40e-05	0-5%
200.0	Au+Au	-1.68e-03 ± 1.12e-05	-1.70e-03 ± 8.38e-06	0-5%
4.5	Au+Au	-8.52e-03 ± 3.57e-04	-9.29e-03 ± 2.33e-04	0-10%
3.0	$\rm Au_{like}$+Al	-3.76e-02 ± 1.53e-03	-7.51e-02 ± 1.16e-03	0-10%
3.5	$\rm Au_{like}$+Al	-2.66e-02 ± 1.17e-03	-2.58e-02 ± 1.01e-03	0-10%
3.9	$\rm Au_{like}$+Al	-1.34e-02 ± 7.50e-04	-1.86e-02 ± 6.03e-04	0-10%
4.5	$\rm Au_{like}$+Al	-1.89e-02 ± 1.22e-03	-2.08e-02 ± 8.39e-04	0-10%

TABLE V. Result for $\nu_{\rm dyn,+-}$ calculated directly (Method 1) or bin-by-bin (Method 2). See text for details.

Au+Au $\sqrt{s_{\rm NN}}$ (GeV)	$< + >$	$< - >$
7.7	91.48	60.11
11.5	135.40	108.74
14.5	135.90	114.49
19.6	161.22	140.76
27	168.08	153.75
39	174.62	163.09
62.4	186.98	178.72
200	228.20	224.59

TABLE VI. Collider mode identified particle numbers used in the $\nu_{\rm dyn}$ calculation, 0-5% centrality only.

$\sqrt{s_{\rm NN}}$ (GeV)	Species	$< + >$	$< - >$
3.0	$\rm Au_{like}$+Al	6.02	1.75
3.5	$\rm Au_{like}$+Al	6.61	2.36
3.9	$\rm Au_{like}$+Al	8.13	3.80
4.5	$\rm Au_{like}$+Al	7.36	3.04
4.5	Au+Au	31.60	19.84
4.9	Al+Au	28.21	11.80

TABLE VII. Fixed target mode identified particle numbers used in the $\nu_{\rm dyn}$ calculation, 0-10% centrality only.

$\sqrt{s_{\rm NN}}$ (GeV)	Species [Centrality]	$\nu_{\rm dyn,+-}$	$< + >$	$< - >$
3.5	W+Al [0-10%]	-5.95e-02 ± 2.77e-04	13.15	7.84
3.5	Au+Al [0-10%]	-5.87e-02 ± 1.05e-04	12.99	7.82
3.5	Bi+Al [0-10%]	-5.76e-02 ± 2.74e-04	12.82	7.83

TABLE VIII. Atomic number (Z-) dependence of $\nu_{\rm dyn,+-}$ from UrQMD in W+Al, Au+Al, and Bi+Al 0-10% most central collisions at $\sqrt{s_{\rm NN}} = 3.5$ GeV.

VI. NET-CHARGE NUMBER FLUCTUATIONS

A. Atomic Number Dependence of $\nu_{\rm dyn,+-}$

Because the beam pipe collisions might involve fragments with an atomic number (Z) less than that of Au, UrQMD was used to investigate the Z-dependence of $\nu_{\rm dyn,+-}$. Table **??**s results for $\nu_{\rm dyn,+-}$ calculated from UrQMD simulations of W+Al, Au+Al, and Bi+Al collisions in the same acceptance as the experimental results. $\nu_{\rm dyn,+-}$ in the most central (0-10%) collisions are calculated and the mean values differ from one another by between 1-2%. Tungsten has Z=74 and bismuth Z=83, so changes of Z between 5-10% only change the mean value of $\nu_{\rm dyn,+-}$ by 1-2%. The conclusion from this study is that the experimentally measured charge fluctuations are insensitive to what heavy fragment is hitting the beam pipe to within 10% in Z of an $\rm Au^{79+}$ ion. This is well within the current experimental precision.

$\sqrt{s_{\rm NN}}$ (GeV)	Species	$\nu_{\rm dyn,+-}$, All v_z	$\nu_{\rm dyn,+-}$, $+v_z$	$\nu_{\rm dyn,+-}$, $-v_z$
3.0	$Au_{\rm like}$+Al	-3.76e-02 ± 1.53e-03 (6.08e05)	-4.05e-02 ± 2.56e-03 (1.92e05)	-3.68e-02 ± 1.32e-03 (4.15
3.5	$Au_{\rm like}$+Al	-2.66e-02 ± 1.17e-03 (4.63e05)	-2.64e-02 ± 2.93e-03 (1.76e05)	-2.64e-02 ± 1.37e-03 (2.87
4.5	$Au_{\rm like}$+Al	-1.89e-02 ± 1.22e-03 (5.18e05)	-2.09e-02 ± 5.51e-04 (3.24e05)	-1.69e-02 ± 1.42e-03 (1.94

TABLE IX. Result for $\nu_{\rm dyn,+-}$ in $Au_{\rm like}$+Al collisions, calculated using the entire v_z range, or positive/negative v_z ranges separately.

$\sqrt{s_{\rm NN}}$ (GeV)	Species	$\nu_{\rm dyn,+-}$, $100 < \lvert v_z\rvert < 200$ cm	$\nu_{\rm dyn,+-}$, $-200 < v_z < -100$ cm	$\nu_{\rm dyn,+-}$, $100 < v_z < 200$ cm
3.0	$Au_{\rm like}$+Al	-3.71e-02 ± 2.56e-03 (5.57e05 events)	-3.66e-02 ± 1.06e-03 (3.88e05 events)	-3.92e-02 ± 2.39e-03 (1.70e05 events)
3.5	$Au_{\rm like}$+Al	-2.74e-02 ± 1.40e-03 (4.30e05 events)	-2.68e-02 ± 1.79e-03 (2.71e05 events)	-2.84e-02 ± 1.96e-03 (1.59e05 events)
4.5	$Au_{\rm like}$+Al	-1.91e-02 ± 4.46e-04 (4.92e05 events)	-1.63e-02 ± 9.13e-04 (1.85e05 events)	-2.14e-02 ± 1.30e-03 (3.06e05 events)

TABLE X. Result for $\nu_{\rm dyn,+-}$ in $Au_{\rm like}$+Al collisions, for different v_z ranges.

VII. SYSTEMATIC ERRORS

Systematic errors for $\nu_{\rm dyn,+-}$ were estimated in a few ways. The differences between the result for TPC-only particle identification (PID) was compared with the TPC+TOF PID. For Au_{like}+Al collisions it was additionally possible to have two independent data samples: one from events with positive v_z and the other with negative v_z.

The results do not exhibit a dependence on transverse momentum, particle detection efficiency, or geometric acceptance. Figures 4, 5, and 6 show the purity of particles when identified with TPC dE/dx, compared to the TOF identification via m^2 measurements. Figure 4 shows the TOF m^2 distribution for pions identified using TPC dE/dx, Figure 5 shows the TOF m^2 distribution for kaons identified using TPC dE/dx, and Figure 6 shows the TOF m^2 distribution for protons identified using TPC dE/dx. Pions identified via TPC energy loss are mainly confirmed to be pions by TOF m^2 measurements. There is some minor misidentification for TPC dE/dx protons, but non-negligible pion contamination of

the dE/dx identified kaons, particularly above 0.5 GeV/c in momentum. For dE/dx kaons and pions used in the analysis, the momentum cuts are $p_T > 0.2$, $p < 0.6$ GeV/c. Higher momenta particles are exclusively identified using TOF.

These estimates are carried out by comparing the particles identified by TOF to those misidentified by TPC dE/dx. If a particle reaches the TOF, it is assumed to be perfectly identified. With the particle identified by TOF, the dE/dx information from the TPC for the same particle/track can be compared to the TOF identification. The primary cross-contamination of particles occurs for pions and kaons due to the relative proximity of the two dE/dx bands. A ratio can be constructed for particles identified by TPC dE/dx as a kaon, while the TOF identifies it as a pion. Under the assumption that the TOF identification is 100% "correct", the ratio of $\frac{TPC(K)==TOF(\pi)}{TPC(K)==TOF(K)}$ provides an estimate of misidentified kaons. Because the TOF has low efficiency for low-p_T tracks, the previous ratio needs to be calculated in different p_T bins and a weighted average can then be calculated using identified kaon spectra from TPC dE/dx. At $\sqrt{s_{NN}} = 7.7$ GeV the ratio of misidentified kaons using TPC dE/dx alone is 17%. At the same energy, but using a combination of TPC+TOF identification decreases the misidentification ratio to 4%. Again, the main assumption in this exercise is that the TOF has "perfect" particle identification. One can see from Figure 3 that this assumption is best for particles with momentum $p < 1.0$ GeV/c, where most of the particle yield lies. The misidentification of kaons as pions tends to increase the value of $\nu_{dyn,K/\pi}$, with increasing pion contamination leading to larger values.

As expected, inclusion of particle identification information from the TOF substantially improves the purity of the identified particles being measured. The TOF also provides the ability to independently perform the analysis without using TPC dE/dx. Results for particle ratio fluctuations calculated using TPC-only or TOF-only particle identification are self consistent. This capability to cross-check particle ratio fluctuations in the energy range from $\sqrt{s_{NN}} = 7.7$-200 GeV using two independent detectors is a unique feature of STAR.

VIII. EVENT QA PLOTS

Included in this section are representative plots of various event-wise and track-wise quantities from Au_{like}+Al and Au+AuFXT events.

Dip angle (θ) is the angle between the momentum of a track and its drift direction,

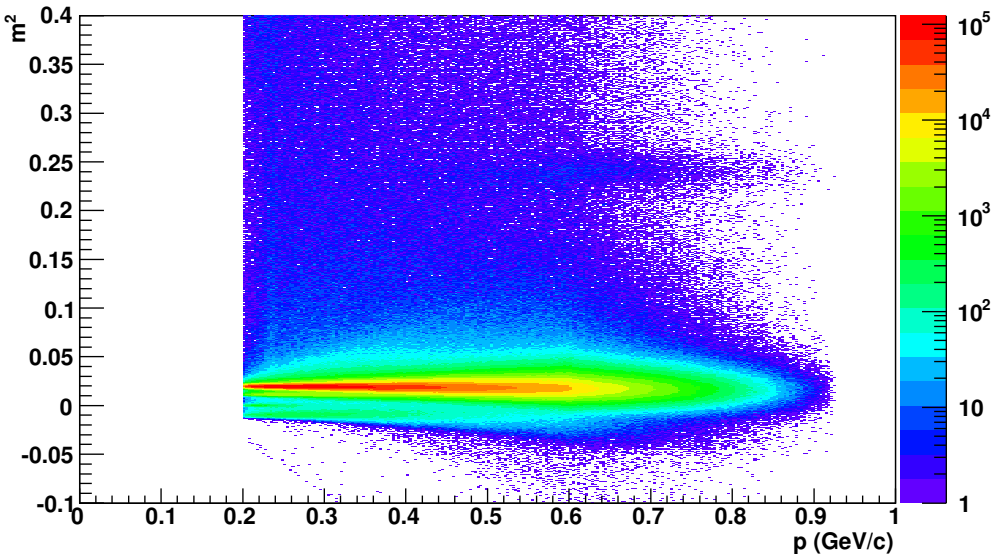

FIG. 4. The mass^2 distribution from the STAR TOF for particles identified as pions via TPC dE/dx. The majority of dE/dx identified pions are confirmed as pions by the TOF. In this analysis, the momentum range for dE/dx identified pions is $p_T > 0.2$, $p < 0.6$ GeV/c.

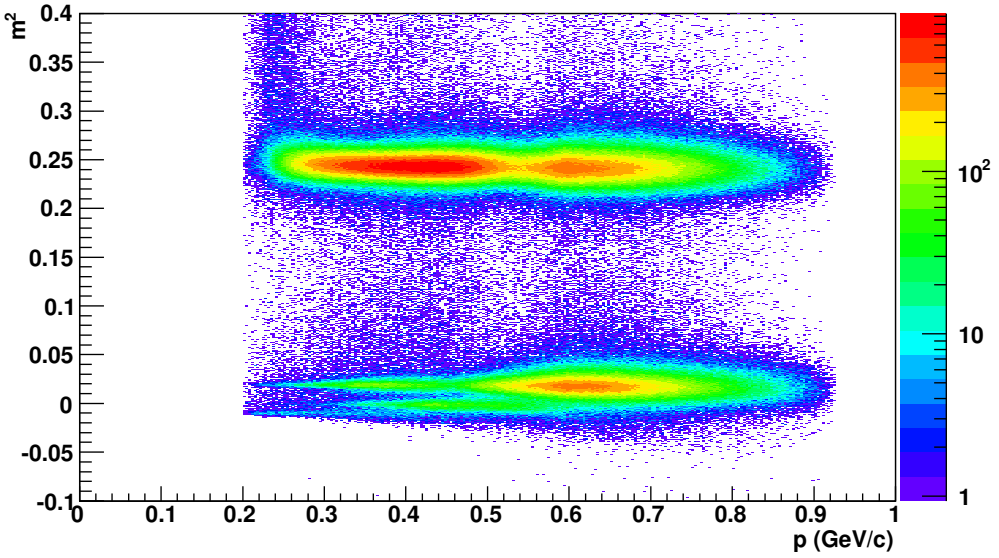

FIG. 5. The mass^2 distribution from the STAR TOF for particles identified as kaons via TPC dE/dx. There is visible contamination in the dE/dx identified kaon sample from pions ($m^2 < 0.06$), which is worse for $p > 0.6$ GeV/c due to the overlap of the pion and kaon dE/dx bands. In this analysis, the momentum range for dE/dx identified kaons is $p_T > 0.2$, $p < 0.6$ GeV/c.

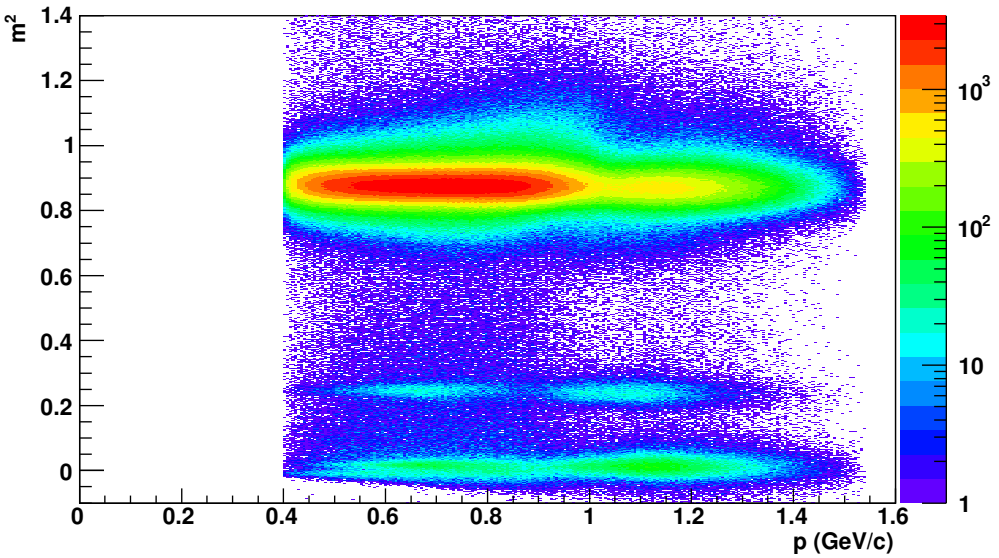

FIG. 6. The mass^2 distribution from the STAR TOF for particles identified as protons via TPC dE/dx. There is minimal contamination in the dE/dx identified proton sample from pions or kaons. In this analysis, the momentum range for dE/dx identified protons is $p_T > 0.4$, $p < 1.0$ GeV/c.

Source of Error	Relative Contribution (Percent)	Method
Electron contamination	1.5 (3.0 GeV) 2 (7.7 and 200 GeV)	Exclude electrons using dE/dx
Straight TOF m^2 Cuts	1(7.7 GeV)-2(200 GeV)	Non-p_T dependent cuts
TPC-only PID	2 (7.7 and 200 GeV)-10	TPC dE/dx only
PID Method	3	dE/dx alone vs dE/dx + TOF
PID Method	≈ 1	dE/dx alone vs dE/dx + TOF
PID Method	≈ 1	dE/dx alone vs dE/dx + TOF

TABLE XI. Summary of studies of main sources of systematic error.

$\theta = cos^{-1}\left(\frac{p_T}{p}\right)$

The v_Z distribution from Au_{like}+Al collisions at $\sqrt{s_{NN}} = 3.9$ GeV shows the reason for instability in the calculated charge fluctuations. The additional material burden added around the beam pipe flanges are clearly visible. Total multiplicities at from Au_{like}+Al collisions at $\sqrt{s_{NN}} = 3.9$ GeV are also higher than that seen from similar collisions at from

$\sqrt{s_{\rm NN}}$ (GeV)	Species	$\nu_{\rm dyn,+-}$ 0-5%	$\nu_{\rm dyn,+-}$ 0-10%	Percent Difference
7.7	Au+Au	-5.40e-03 ± 5.50e-05	-5.45e-03 ± 6.40e-05	0-5%
11.5	Au+Au	-4.23e-03 ± 5.42e-05	-4.29e-03 ± 3.67e-05	0-5%
14.5	Au+Au	-3.76e-03 ± 2.26e-05	-3.80e-03 ± 3.54e-05	0-5%
19.6	Au+Au	-3.39e-03 ± 1.57e-05	-3.47e-03 ± 2.22e-05	0-5%
27.0	Au+Au	-3.03e-03 ± 1.51e-05	-3.05e-03 ± 1.34e-05	0-5%
39.0	Au+Au	-2.66e-03 ± 2.66e-05	-2.68e-03 ± 1.93e-05	0-5%
62.4	Au+Au	-2.38e-03 ± 4.31e-05	-2.41e-03 ± 2.40e-05	0-5%
200.0	Au+Au	-1.68e-03 ± 1.12e-05	-1.70e-03 ± 8.38e-06	0-5%
4.5	Au+Au	-8.52e-03 ± 3.57e-04	-9.29e-03 ± 2.33e-04	0-10%
3.0	$\rm Au_{like}$+Al	-3.76e-02 ± 1.53e-03	-7.51e-02 ± 1.16e-03	0-10%
3.5	$\rm Au_{like}$+Al	-2.66e-02 ± 1.17e-03	-2.58e-02 ± 1.01e-03	0-10%
3.9	$\rm Au_{like}$+Al	-1.34e-02 ± 7.50e-04	-1.86e-02 ± 6.03e-04	0-10%
4.5	$\rm Au_{like}$+Al	-1.89e-02 ± 1.22e-03	-2.08e-02 ± 8.39e-04	0-10%

TABLE XII. Result for $\nu_{\rm dyn,+-}$ (0-5%) vs 0-10%.

$\rm Au_{like}$+Al collisions at $\sqrt{s_{\rm NN}} = 4.5$ GeV.

At low energies the majority of produced particles are pions and protons. There are very few kaons and anti-protons prouced. An earlier STAR analysis (STAR FXT Coulomb Effect paper) used $\rm Au_{like}$+Al collisions fixed target data. UrQMD studies were carried out to determine the observable that best corresponds to centrality at low energies. Ultimately, collision centrality was defined in terms of only produced particles (pions) to avoid knockout protons and spectator particles. In Au/Al+AuFXT data at $\sqrt{s_{\rm NN}} = 4.5$ and 4.9 GeV, total charged particle multiplicity was well enough defined to be used for centrality determintion.

[1] B. Alver *et al.* (PHOBOS Collaboration), Phys. Rev. **C83**, 024913 (2011).

[2] K. Aamodt *et al.* (ALICE Collaboration), Phys. Rev. Lett. **105**, 252301 (2010).

[3] A. Adare *et al.* (PHENIX Collaboration), Phys. Rev. **C93**, 024901 (2016).

[4] K. Aamodt *et al.* (ALICE Collaboration), Phys. Rev. Lett. **106**, 032301 (2011).

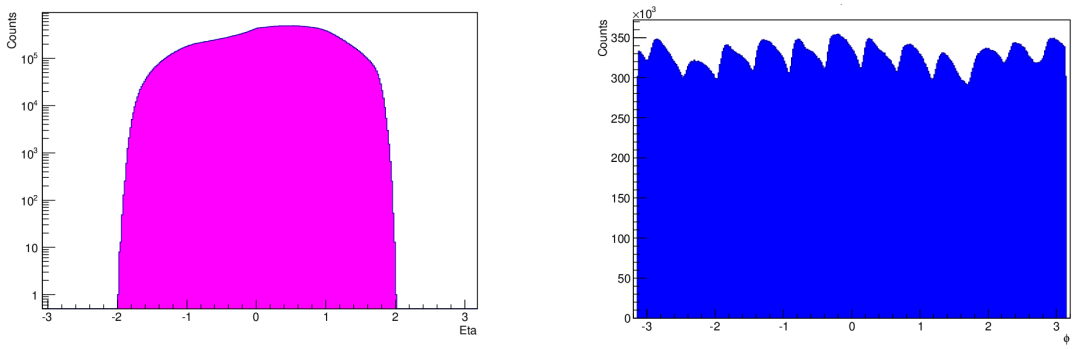

(a) (b)

FIG. 7. TPC track pseudorapidity (η, 7(a)) and angular (ϕ, 7(b)) distributions from Au_{like}+Al collisions at $\sqrt{s_{NN}} = 3.0$ GeV.

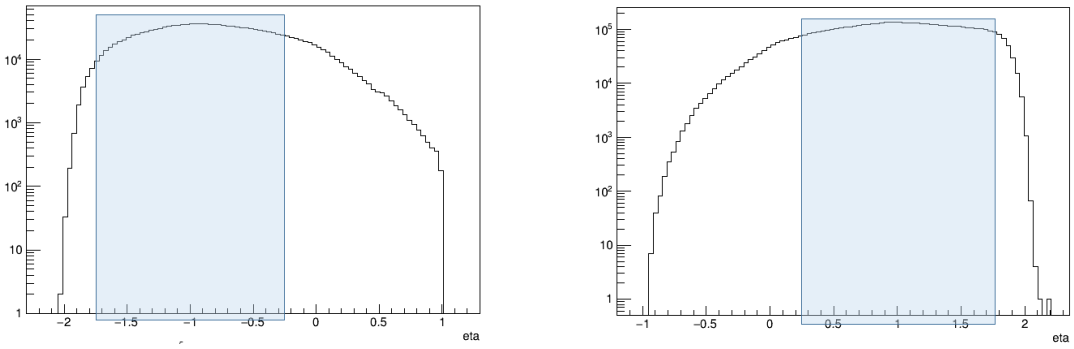

(a) (b)

FIG. 8. TPC eta (η) distributions for events with either positive (8(a)) or negative (8(b)) v_Z from Au_{like}+Al collisions at $\sqrt{s_{NN}} = 3.0$ GeV.

[5] C. Loizides, J. Nagle, and P. Steinberg, SoftwareX **1-2**, 13 (2015).

[6] B. Abelev (STAR Collaboration), Phys. Rev. Lett. **103**, 172301 ((2009)).

[7] P. Christiansen, E. Haslum, and E. Stenlund, Phys. Rev. **C80**, 034903 (2009).

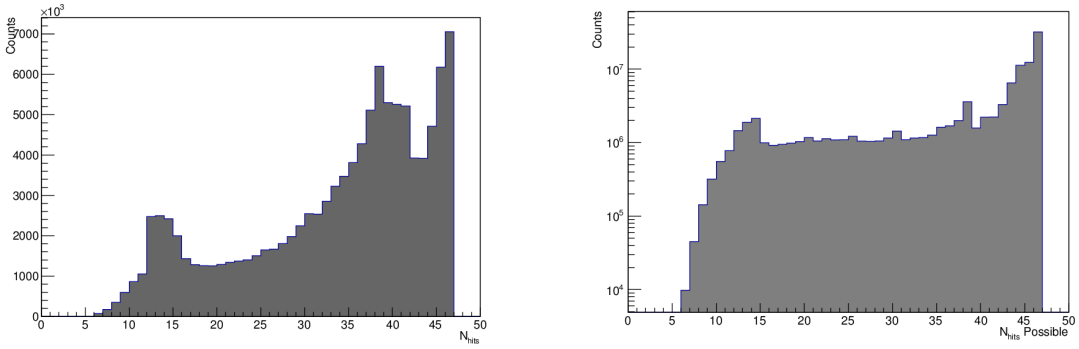

(a) (b)

FIG. 9. TPC track fit points (N_{fit}, 10(a)) and fit points possible (N_{poss}, 10(b)) distribution from Au_{like}+Al collisions at $\sqrt{s_{NN}} = 3.0$ GeV.

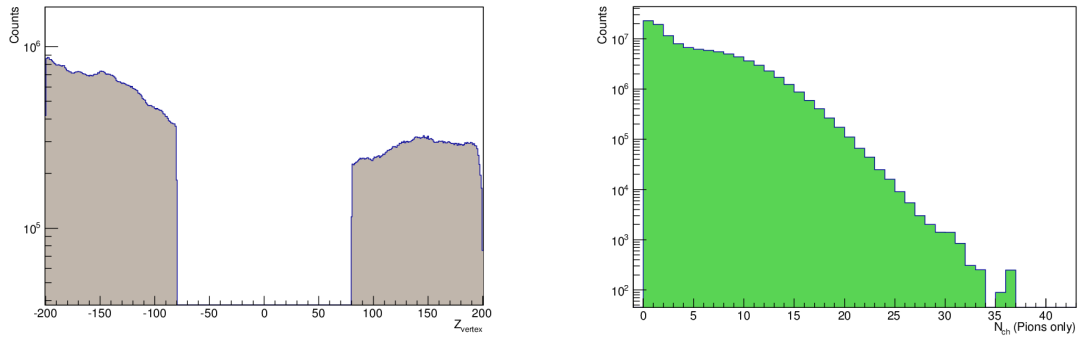

(a) (b)

FIG. 10. Z-vertex (v_Z) and pion multiplicity distributions in the range $|\eta - y_{cm}| < 0.5$from Au_{like}+Al collisions at $\sqrt{s_{NN}} = 3.0$ GeV.

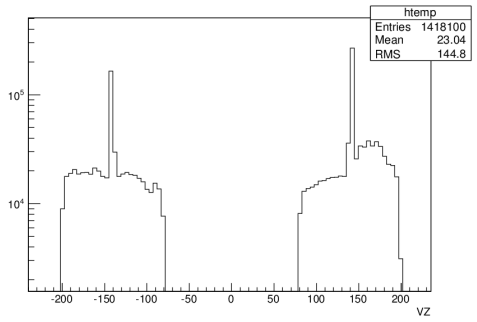

FIG. 11. Z-vertex (v_Z) distribution from Au_{like}+Al collisions at $\sqrt{s_{NN}} = 3.9$ GeV.

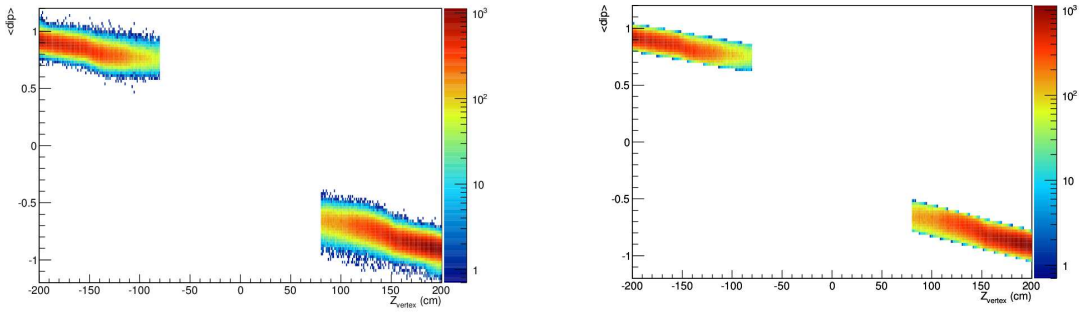

(a) (b)

FIG. 12. Track dip angle as a function of Z-vertex (v_Z) for 0-10% collisions from Au_{like}+Al at $\sqrt{s_{NN}}$ = 4.5 GeV, before (12(a)) and after (12(b)) a 2σ cut.

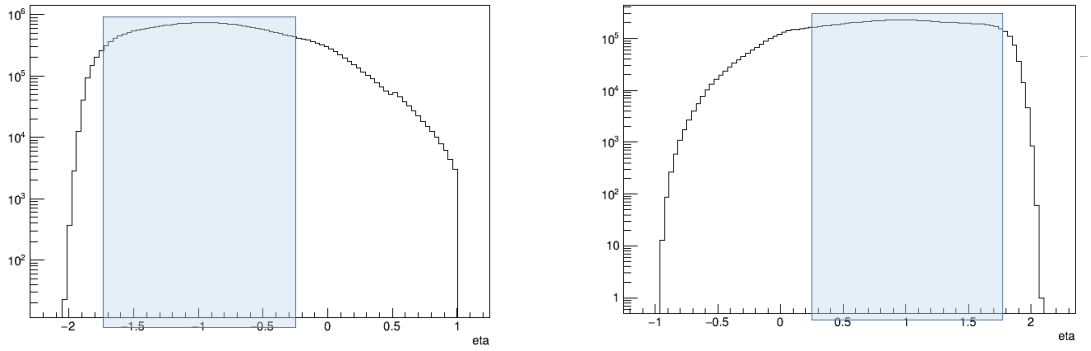

(a) (b)

FIG. 13. TPC eta (η) distributions for events with either positive (13(a)) or negative (13(b)) $v_Z$from Au_{like}+Al collisions at $\sqrt{s_{NN}}$ = 4.5 GeV.

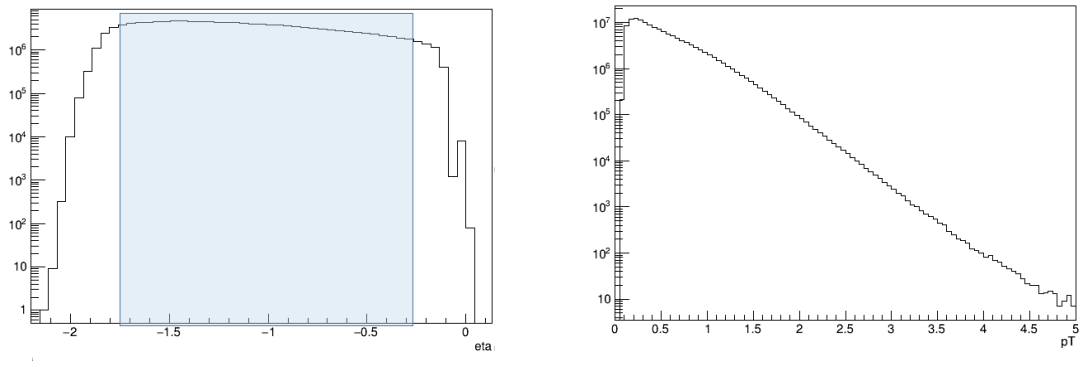

(a) (b)

FIG. 14. TPC track pseudorapidity (η, 14(a)) and transverse momentum (p_T, 14(b)) distributions from Au+Au collisions at $\sqrt{s_{NN}} = 4.5$ GeV.

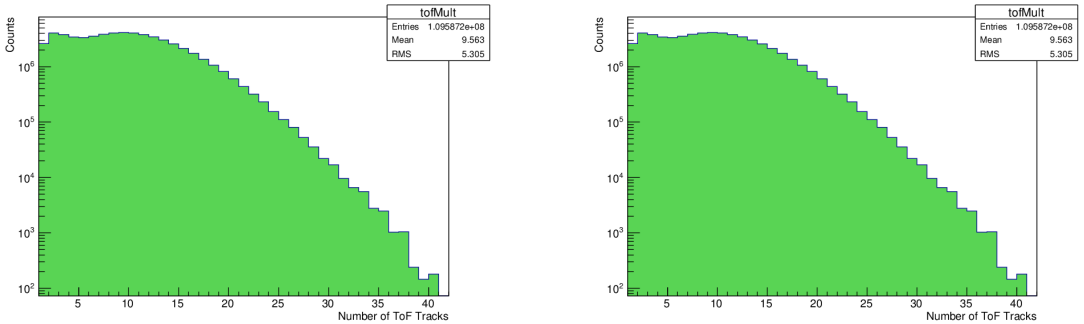

(a) (b)

FIG. 15. Number of TOF tracks distribution from Au_{like}+Al collisions at $\sqrt{s_{NN}} = 3.0$ GeV.